

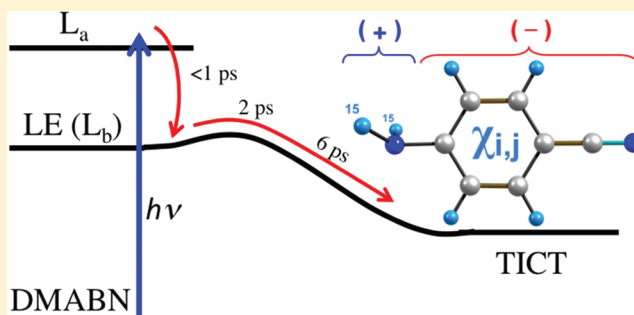
Multimode Charge-Transfer Dynamics of 4-(Dimethylamino)benzonitrile Probed with Ultraviolet Femtosecond Stimulated Raman Spectroscopy

Justin M. Rhinehart, J. Reddy Challa, and David W. McCamant*

Department of Chemistry, University of Rochester, Rochester, New York 14627-0216, United States

S Supporting Information

ABSTRACT: 4-(Dimethylamino)benzonitrile (DMABN) has been one of the most studied photoinduced charge-transfer (CT) compounds for over 50 years, but due to the complexity of its excited electronic states and the importance of both intramolecular and solvent reorganization, the detailed microscopic mechanism of the CT is still debated. In this work, we have probed the ultrafast intramolecular CT process of DMABN in methanol using broad-band transient absorption spectroscopy from 280 to 620 nm and ultraviolet femtosecond stimulated Raman spectroscopy (FSRS) incorporating a 330 nm Raman pump pulse. Global analysis of the transient absorption kinetics revealed dynamics occurring with three distinct time constants: relaxation from the Franck–Condon L_a state to the lower locally excited (LE) L_b state in 0.3 ps, internal conversion in 2–2.4 ps that produces a vibrationally hot CT state, and vibrational relaxation within the CT state occurring in 6 ps. The 330 nm FSRS spectra established the dynamics along three vibrational coordinates: the ring-breathing stretch, ν_{ph} , at 764 cm^{-1} in the CT state; the quinoidal C=C stretch, ν_{CC} , at 1582 cm^{-1} in the CT state; and the nitrile stretch, ν_{CN} , at 2096 cm^{-1} in the CT state. FSRS spectra collected with a 400 nm Raman pump probed the dynamics of the 1174 cm^{-1} CH bending vibration, δ_{CH} . Spectral shifts of each of these modes occur on the 2–20 ps time scale and were analyzed in terms of the vibrational anharmonicity of the CT state, calculated using density functional theory. The frequencies of the δ_{CH} and ν_{CC} modes upshift with a 6–7 ps time constant, consistent with their off-diagonal anharmonic coupling to other modes that act as receiving modes during the CT process and then cool in 6–7 ps. It was found that the spectral down-shifts of the δ_{CH} and ν_{CN} modes are inconsistent with vibrational anharmonicity and are instead due to changes in molecular structure and hydrogen bonding that occur as the molecule relaxes within the CT state potential energy surface.



INTRODUCTION

4-(Dimethylamino)benzonitrile (DMABN, Figure 1) is the archetypical “push–pull” chromophore that experiences a dramatic photoinduced charge transfer (CT) in the excited state after absorbing ultraviolet light. The mechanism of the CT process has been studied for over 50 years, since the original fluorescence experiments by Lippert, and a detailed description of the mechanism still remains elusive.^{1–3} The siren song of this research, which has kept the field active for such a long time, is DMABN’s compact structure which belies an extremely complicated electronic state manifold but gives one the impression that we ought to be able to establish a complete description of the structural dynamics that drive the CT process. Such a description should encompass both DMABN’s structural changes and the solvent reorganization during CT. In the pursuit of this description, DMABN has been theoretically modeled and experimentally probed using both electronic and vibrational spectroscopy.

A schematic of the current understanding of DMABN’s CT process is shown in Figure 1.^{3,4} Optical excitation places the molecule on the Franck–Condon surface of S_2 , in the

well-known L_a ($\pi\pi^*$) electronic state of benzene derivatives. The L_a state relaxes in less than a picosecond to a slightly lower energy L_b state, termed the locally excited (LE) state, from which the high-energy “B” fluorescence originates. Through fluorescence anisotropy measurements, fluorescence is known to occur from the energetically lower L_b state, whereas photoexcitation directly populates the higher oscillator strength L_a state. Over the next 5–10 ps, the LE state relaxes to the twisted intramolecular CT (TICT) state that is characterized by a 90° twist of the amine relative to the benzene ring, as well as a quinoidal contraction of the benzene ring. A lower energy “A” fluorescence band arises from the CT \rightarrow ground state emission. The dual fluorescence from the LE and CT states makes DMABN amenable to a huge variety of physical organic chemistry experiments in which the structure of the molecule is

Special Issue: Richard A. Mathies Festschrift

Received: March 2, 2012

Revised: April 24, 2012

Published: April 26, 2012

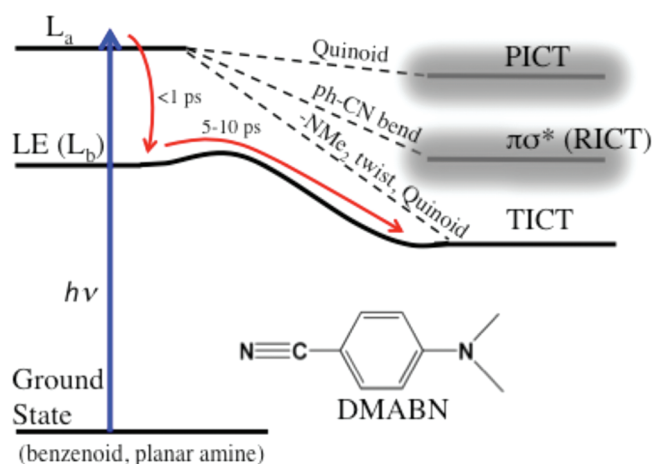


Figure 1. Schematic energy levels of DMABN. L_a and $LE (L_b)$ states correspond to $\pi\pi^*$ excitations of the benzene ring. The $\pi\pi^*$ manifold is connected to a variety of different CT states by different geometric distortions. These include the planar intramolecular CT state (PICT), characterized by a quinoidal benzene ring and amine in the plane of the ring; the $\pi\sigma^*$ or rehybridized intramolecular CT state (RICT) with a distinctive bent ph-CN angle; and the twisted intramolecular CT state (TICT) that contains a quinoidal benzene ring and an amine that is twisted perpendicular to the ring.

subtly changed and the relative intensity of the two bands monitored.³⁻⁷

As shown in Figure 1, theoretical studies using a variety of quantum mechanical methods have revealed the presence of several other electronic states in close proximity to the L_a , LE , and TICT states. These studies were summarized in more detail in our previous publication but will be outlined here.⁸ A planar intramolecular CT (PICT) state has been shown to lie near the Franck–Condon structure in a vacuum, and this state may be particularly relevant in derivatives with nonrotating amine substituents.^{5,9-12} The PICT state is typically characterized by a valence bond resonance structure in which the benzene ring is quinoidal and a strong pi-bond exists between the phenyl and amine, as well as between the phenyl and the nitrile carbon. In polar solvents, the twist of the amine increases the dipole moment of the excited state significantly and thereby lowers the energy and stabilizes the TICT state relative to the PICT state, though in some calculations the TICT energy remains below PICT even in a vacuum.^{10,12} The PICT model of the CT state has been predicted to have a reduced frequency of the nitrile stretch and a quinoidal benzene configuration.^{11,13-18} Interestingly, both of these have been observed in the fully relaxed CT state, along with definitive indications that the amine is twisted, indicated by the downshift of the ph-N stretching frequency in the CT state.^{16,19} Overall, this paints a picture of a relaxed TICT state with both a twisted amine group and a quinoidal benzonitrile group.^{9,11,12}

Lim et al. has advocated for the existence of a $\pi\sigma^*$ state that forms as an intermediate prior to the TICT state, a proposal that has been a source of significant recent debate.²⁰⁻²⁶ The $\pi\sigma^*$ state, previously known as the rehybridized ICT or RICT state, is characterized by the promotion of an electron into the σ^* orbital on the nitrile from the π orbital within the aromatic ring. This process is accompanied by a bending of the nitrile substituent. Time-dependent density functional theory (TDDFT) was used to assign different regions of the transient absorption spectrum to either the TICT state, the LE state, or

the $\pi\sigma^*$ state.²¹ The differing kinetics of these different regions was interpreted as being consistent with a branching of the L_a population into either the $LE (L_b)$ state or the $\pi\sigma^*$ state, with the $\pi\sigma^*$ state being a fleetingly populated precursor to the TICT state.^{21,25} However, this interpretation depends on an extraordinary solvation energy that rapidly stabilizes the highly dipolar $\pi\sigma^*$ state and the experimental interpretation is hampered by the reliance on the TDDFT assignment which is known to produce unreliable energies for systems with significant CT character. Additional work by Zachariasse discussed problems with the $\pi\sigma^*$ transient absorption interpretation and pointed out some problems in the fluorescence data.²⁷

Most experimental work on DMABN has focused on steady-state and time-resolved electronic spectroscopies, such as fluorescence and femtosecond transient absorption (TA).^{3,7,21,25,27-29} These methods have established the kinetics of CT but are inherently insensitive to the changes in molecular structure along the reaction path. Instead, vibrational spectroscopy has a natural sensitivity to subtle changes in molecular structure and has been the primary tool by which structural details have been mapped onto the reaction coordinate.^{17,19,30-35} Both time-resolved infrared (TRIR) and transient Raman studies, collected at 16 or 50 ps after photoexcitation, have definitively established the twisted, quinoidal structure of the relaxed CT state.^{19,31} However, there have been only a few studies of the evolution of the vibrational spectrum over time, which can illuminate the structural deformations that move the molecule from the LE to CT state. Among these are the TRIR work of Okamoto, who studied the changes in the spectrum of an analogous compound with 4 ps time resolution, and Kwok, who focused on the evolution of the nitrile spectrum with 0.2 ps time resolution.^{17,33-35} Okamoto observed the time-dependent frequencies of the 1219 and 964 cm^{-1} peaks, which was ascribed to different vibrational relaxation rates of the two modes.¹⁷ Kwok showed that the nitrile vibration grows on the ~ 5 ps time scale and experiences very little spectral shift. In hydrogen bonding solvents, Kwok observed the initial appearance of a dramatically downshifted nitrile vibration at 2109 cm^{-1} and the subsequent growth of a further down-shifted nitrile at 2091 cm^{-1} that was assigned to a hydrogen-bonded ICT state (HICT). The equilibration of both peaks with a 13 ps time constant was attributed to a rapid equilibrium established between hydrogen-bonded and non-hydrogen-bonded species.³³⁻³⁵ In that work, the loss of intensity in the CT state's nitrile peaks and the recovery of the ground-state bleach indicated that the hydrogen bonding environment produced a 5-fold acceleration in the internal conversion to the ground state.³³ Thus, in acetonitrile, the singlet CT-state lifetime is ~ 2.7 ns and is predominantly quenched by intersystem crossing to the triplet CT state (81% triplet yield), whereas, in methanol, the CT-state lifetime is reduced to 1.6 ns and only $\sim 50\%$ of the singlet CT state population relaxes via intersystem crossing, with the remaining 50% returning to the ground state.³³

To this body of work, we added our previous femtosecond stimulated Raman spectroscopy (FSRS) study of DMABN in methanol.⁸ Over the past decade, FSRS has been developed by Mathies and others as a new spectroscopic tool for photochemistry that offers excellent time and frequency resolved Raman spectra devoid of problematic fluorescent backgrounds.^{8,36-45} In our previous DMABN work, we used FSRS to observe the dramatic spectral shift of the CT state's 1582 cm^{-1} quinoidal C=C stretching vibration, which occurred with a 6 ps time constant. The 12 cm^{-1} shift of that peak was

attributed to off-diagonal coupling to other receiving modes that were excited by the CT process. However, the 400 nm Raman pump used in the previous work was only able to probe vibrational modes confined to the phenyl ring because of the orientation of the 400 nm transition dipole in the CT state.³² By using a Raman-pump wavelength that is resonant with the CT state's 330 nm absorption band, whose transition dipole is parallel to the long molecular axis, a variety of different vibrational modes are observable.¹⁹ These results have been complimented with density functional theory (DFT) anharmonic coupling calculations in an effort to follow the structural dynamics along the CT reaction coordinate. In addition, TA spectra extending further into the ultraviolet have been recorded in order to establish the overall kinetics of the CT reaction in methanol.

EXPERIMENTAL SECTION

The femtosecond stimulated Raman and transient absorption (TA) spectra presented here utilized the 800 nm, 100 fs fundamental output of a Ti:sapphire regenerative amplifier (Spectra-Physics Spitfire) with a 1 kHz repetition rate. The 266 nm actinic pump pulse used for the TA experiments was generated from the third harmonic of the Ti:sapphire fundamental. Pump powers of 0.40 and 0.90 mW were used for the UV and visible TA regions, respectively. The 330 nm, 4.0 μ J Raman pump pulse was produced by a narrow bandwidth near-infrared optical parametric amplifier, with subsequent fourth harmonic generation (Quantronix Palitra ps) resulting in a 0.65 ps pulse duration. The 400 nm, 1.0 μ J Raman pump pulse was created from spectrally filtering the fundamental output of the Ti:sapphire and then frequency-doubling in a 3 mm BBO crystal, resulting in a narrow bandwidth, 2 ps pulse. The white-light continuum probe was produced by either (1) frequency doubling a small portion of the Ti:sapphire fundamental output and then focusing the resultant 400 nm beam into a CaF₂ crystal or (2) using the fundamental 800 nm output of the Ti:sapphire directly and focusing it into a CaF₂ crystal. The 400 nm/CaF₂ generated probe pulse was used for UV TA (260–370 nm) and FSRS spectra that utilized the 330 nm Raman pump pulse. The 800 nm/CaF₂ generated probe pulse was used for the 330–640 nm TA and the 400 nm FSRS spectra. Beams were focused onto the sample by a 100 mm focal length curved mirror, producing ~ 40 μ m diameter beams at the sample. After the sample, the probe was dispersed with a grating spectrograph and directed into a CCD camera (Princeton Instruments Pixis 100BR) that was read out at 1 kHz using LabView (National Instruments). Alignment of the pump and probe polarizations at the magic angle (54.7°) eliminated signatures from rotational diffusion. DMABN (Aldrich) was used as received, and purity was confirmed by NMR analysis. Methanol (Mallinckrodt Chemicals) was spectroscopic grade and used as received to prepare 6 mM DMABN solutions.

The liquid jet sample apparatus was open to air and flowed in a wire-guided vertical "sheet" of approximately 150–200 μ m thickness.⁴⁶ The UV TA spectra (region of 260–370 nm) are the result of averaging 1600 spectra per time point where the actinic pump pulse was chopped at 500 Hz. Pump–probe time delays were stepped linearly between –1 and 1 ps and logarithmically at longer delays.⁴⁷ The visible TA spectra (330–640 nm) are the result of averaging 1000 spectra per time point with similar linear and logarithmic time spacing.

The Raman pump and continuum probe pulses obtained a Raman spectrum of the sample as the amplification of the

probe spectrum at Stokes Raman frequencies relative to the Raman pump wavelength.^{36,38,48} Ground state and positive time-delay FSRS spectra, for both Raman pump wavelengths, were the result of averaging 10 000 spectra at nine slightly shifted spectrograph positions, giving a total acquisition time of 180 s. This scanning multichannel technique (SMT) was used in order to reduce the systematic pixel-to-pixel variations in sensitivity and improve spectral reproducibility.^{49–51} The positive time-delay FSRS spectra shown were collected by chopping the 266 nm excitation pulse at 500 Hz. The resultant spectrum (D, Figure 2) contains both FSRS difference signals

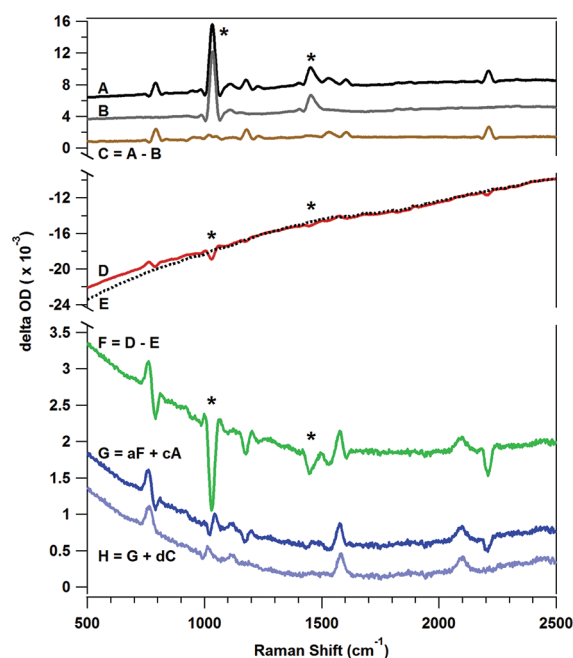


Figure 2. Representative FSRS spectra at 40 ps pump–probe time delay depicting the analysis procedure. Methanol solvent peaks are labeled with asterisks (*). Spectra of ground state DMABN with solvent (A), pure solvent (B), and ground state DMABN with solvent subtracted (C) are shown in the top window. The middle window shows the excited state difference spectrum at 40 ps (D) and the transient-absorption-only spectrum also at 40 ps (E). The bottom window displays the subtraction of the transient background from the positive time-delay spectrum (F), the scaled addition of the ground state with solvent (cA , with $c = 0.142$) to a scaled version of F in order to eliminate the solvent peaks (G), and then finally, the scaled addition of spectrum C to G to eliminate the ground state bleach features (H). This final spectrum (H) was then fit using the analysis procedure outlined in the text. All spectra are offset for clarity except spectra D and E.

and a broad TA background, which was removed by subtraction of a transient-absorption-only spectrum collected under identical conditions but with the Raman pump blocked (E, Figure 2). This spectrum (F) then displays positive excited-state peaks and negative features that occur from both the bleach of the ground state and the attenuated power of the Raman pump. The Raman signal of all ground-state DMABN and solvent peaks is decreased at positive time delays because of DMABN's excited state absorption band around 330 nm, which absorbs the Raman pump and thereby decreases the resulting Raman intensity. This causes the negative signals for the ground state bleach and solvent peaks and also reduced the signal for the transient excited state peaks. In order to correct this, the solvent peaks were used as internal standards. An attenuated ground-state + solvent

spectrum ($0.142 \times A$), collected by chopping the Raman pump in the absence of the 266 nm pump, was added to scaled positive pump–probe spectra ($a \times F$, with “ a ” ranging from 1.18 to 1.30) so that the negative solvent peaks in the transient spectra were removed. This effectively scaled the time-resolved spectra so that each contained equivalent solvent peak intensities. The remaining signals (G) contain only positive features from DMABN’s excited state and negative ground-state DMABN bleaches induced by optical excitation of the sample. As an additional step, a scaled DMABN ground-state spectrum (C) was added into these spectra to eliminate the bleach signals and facilitate analysis of the excited-state peaks without contamination by the distorted line shapes of the ground state (H).

Time resolution and probe chirp for the 330 nm FSRS and UV TA experiments were both determined from optical Kerr effect (OKE) measurements done in the liquid jet apparatus between the 266 nm pump and continuum probe pulses. Fitting the resulting signals to a wavelength dependent Gaussian line shape, the full-width half-maximum of the instrument response function (IRF) was determined to vary between 213 and 274 fs across the spectral range. The probe chirp, measured the same way, showed a 236 fs delay between probe wavelengths of 280 and 360 nm and a delay of 96 fs within the FSRS spectral window. For the FSRS spectra, the spectral resolution was determined to be 26 cm^{-1} , primarily due to the Raman-pump pulse bandwidth. The accuracy of the Raman shift axis is estimated as $\pm 5 \text{ cm}^{-1}$. Time resolution and probe chirp for the 400 nm FSRS and visible TA, also determined via OKE, gave an IRF ranging from 225 to 256 fs across the spectral window (330 to 620 nm). The probe chirp was measured to have a 293 fs delay between 330 and 620 nm and a delay of 40 fs within the FSRS spectral window.

Gaussian 09 software was used for the density functional theory calculations that employed B3LYP methods with various basis sets while performing Barone’s automated methodology for the anharmonic vibrational analysis.^{52–54} Qualitative assignment of the vibrational modes was visualized through the graphical program Chemcraft (<http://www.chemcraftprog.com>) and compared against known DMABN assignments and frequencies.

RESULTS

Time-resolved TA of the UV and visible regions of DMABN in methanol at room temperature can be seen in Figure 3a. The spectra can be broken down into five contributions: (1) a broad absorption band observed from 440 to 640 nm assigned to the LE state; (2) a sharp absorption peak centered at 410 nm assigned to the CT state; (3) the stimulated emission band of the LE state, referred to as LE(SE), that is overlapped with the CT state absorption between wavelengths of ~ 320 and 440 nm; (4) a sharp band at 330 nm assigned to an excited state absorption that is present at all positive pump–probe time delays; and (5) the ground state bleach seen from 270 to 320 nm. Absorption band assignments are in agreement with previous studies of DMABN in acetonitrile^{22,55} and our previous studies of DMABN in methanol.⁸ The broad absorption assigned to the LE state reaches its maximum in the first picosecond and then decays over the next 5–10 ps. On the other hand, the CT absorption band at 410 nm shows growth over this same time range. Druzhinin et al. show that the SE(LE) band for acetonitrile is a broad negative feature centered at $\sim 360 \text{ nm}$.²⁸ Therefore, congruent with its own time-dependent increase in signal intensity, the CT state signal growth loses the overlapping

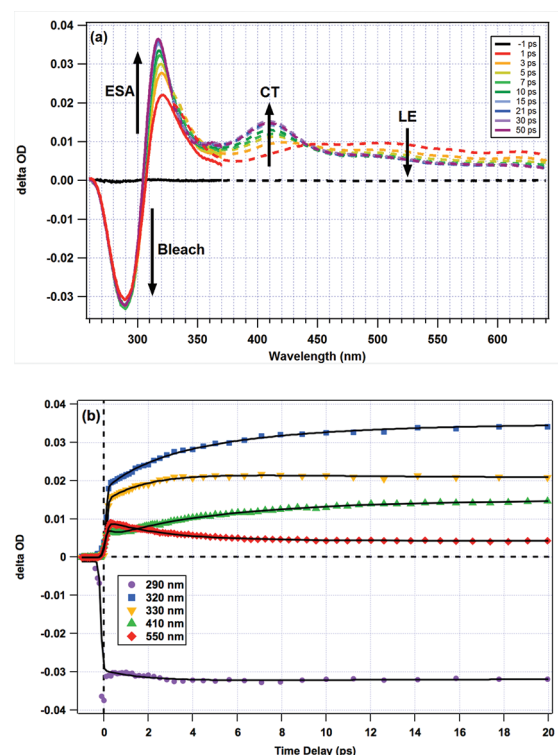


Figure 3. Combined transient absorption for the UV and visible regions. (a) Transient absorption spectra for DMABN in methanol for pump–probe time delays ranging from -1 to 20 ps using a pump wavelength of 266 nm . (b) Kinetic traces for 290 nm (ground state bleach), 320 nm (excited state absorption; ESA), 330 nm (FSRS Raman pump wavelength), 410 nm (charge transfer state; CT), and 550 nm (locally excited state; LE). Trace data shown as points and kinetic fit shown as solid line. For (a), the solid lines represent data from the UV region experiment and the dotted lines data from the visible region experiment. All spectra, kinetic traces, and amplitude values from the visible region data were scaled on the basis of pump power differences between the two experiments.

negative intensity contribution from the SE(LE) band as the pump–probe delay time increases. As expected, the ground state bleach from 270 to 300 nm remains relatively constant at all times, indicating negligible ground state recovery over the first 50 ps .

TA kinetics were analyzed using a global fitting procedure with wavelength-independent time constants and wavelength-dependent amplitudes. Individual kinetic traces were selected at 20 wavelengths. These kinetic traces were then fit simultaneously to a sum of three exponentials with a wavelength dependent zero-of-time and positive time delay offset which was then convoluted with a wavelength dependent instrument response function. The general equation for the global analysis fitting is shown in eq 1.

$$\text{OD}_\lambda(t) = \text{IRF}_\lambda \otimes [A_{0,\lambda} + \sum_{i=1}^3 A_{i,\lambda} e^{-(t-t_{0,i})/\tau_i}] \quad (1)$$

Note that the instrument response function (IRF_λ), positive-time offset ($A_{0,\lambda}$), exponential amplitudes ($A_{i,\lambda}$), and zero-time ($t_{0,i}$) are all functions of wavelength, whereas the time constants (τ_i) are not. Accurate fitting of the kinetics at all 20 wavelengths required the inclusion of three time constants: 0.34 , $2\text{--}2.4$, and 6.5 ps . The collection of decay-associated spectra, $A_{0,i}$, or DAS, is shown in Figure 4 and describes the

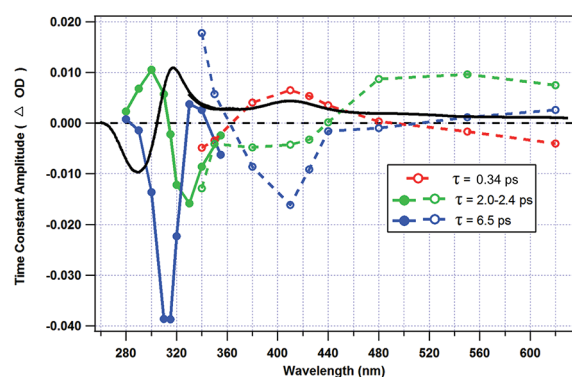


Figure 4. Decay-associated spectra, $A_{0,\lambda}$, from global fit of the spectral kinetics in Figure 3, along with a scaled transient absorption spectrum at 50 ps pump–probe time delay for comparison (black trace). As in Figure 3, solid lines represent data from the UV transient absorption region and dotted lines correspond to the visible region.

overall shape of the kinetics across the spectrum. Comparison of Figures 3a and 4 is a unique analysis tool in determining what spectral changes occur on each time scale. Because of the global approach to the analysis, a complete picture beyond individual wavelength analyses can be drawn and the entire absorption characteristics of the molecule over the investigated time range can be visualized simultaneously.

The 0.34 ps DAS seen in Figure 4 (red) may characterize the fast relaxation within the “LE” state from the initially populated L_a state to the L_b state. The positive amplitude from 380 to 440 nm indicates that this region experiences loss of TA amplitude with a 0.34 ps time constant. Further to the red, the negative amplitude at 620 nm indicates that there is a small growth of signal at this wavelength occurring with a 0.34 ps time constant. The green trace indicates evolution occurring on the 1.96 ps time scale for the UV region and 2.44 ps for the visible region, with positive amplitudes corresponding to decay exponentials and negative amplitudes to growth exponentials. Consistent with expectations from the absorption band assignment, wavelengths greater than 440 nm, assigned to the LE state, experience the majority of their decay with a 2.44 ps time constant (green

dashed traces, Figure 4) with negligible kinetics occurring with a 6.51 ps time constant (blue dashed traces, Figure 4). The absorption band assigned to the CT state, seen primarily between 320 and 440 nm, has a growth of intensity with a 1.96 ps time constant in the UV and a 2.44 ps time constant in the visible and then subsequent sharpening and further growth. Global analysis places this sharpening and growth at 6.51 and 6.50 ps for the UV and visible regions, respectively. The sharp excited-state absorption band centered at 320 nm has significant growth with a 1.96 ps time constant and then a dramatic sharpening with a 6.51 ps time constant, seen by the large negative amplitude of the blue trace at wavelengths below 340 nm.

Using FSRS, a detailed picture of the CT process was obtained via observations of three excited state modes using the 330 nm Raman pump and an additional mode with the 400 nm Raman pump pulse. The time-resolved spectra of the excited state modes (Figures 5 and 6) are shown for $\Delta t = 1$ –40 ps, along with the ground state spectrum for comparison. Assignment of the ground state modes at 792, 1604, and 2213 cm^{-1} to the ring breathing/in-plane phenyl deformation (Wilson mode 12a, ν_{ph}), quinoidal C=C stretching vibration (Wilson mode 8a, ν_{CC}), and nitrile stretch (ν_{CN}), respectively, and the excited state mode at 1174 cm^{-1} to the in-plane C–H bending vibration (δ_{CH}) is in agreement with previous results.^{14,19,56,57} Each mode exhibited a negative ground state bleach feature at its corresponding ground state frequency at positive time delays, but as previously explained, these features were removed for ease of analysis of the excited-state peaks. In comparison to FSRS spectra taken with a 400 nm Raman pump in which the ν_{ph} and ν_{CN} modes were not resonantly enhanced, the 330 nm Raman pump used here is resonant with an excited-state absorption band whose transition dipole is parallel to the long axis of DMABN and so resonance enhancement of these Raman modes is obtained.^{8,19,32,34} Excited state peaks can initially be seen as a broad feature by 2 ps. A more pronounced and sharp feature can be seen after ~ 4 ps. To extract quantitative kinetics, all excited state peaks were fit to the sum of a positive Gaussian and a polynomial baseline.

2096 cm^{-1} , ν_{CN} Mode. In the excited state, the nitrile stretching mode appears downshifted from its ground-state

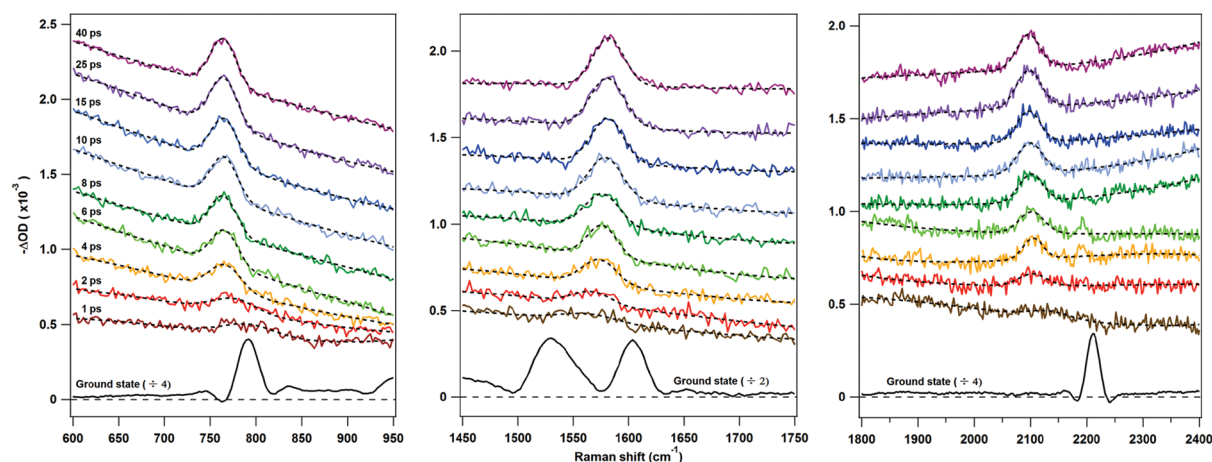


Figure 5. FSRS spectra of DMABN in methanol using a 330 nm Raman pump. Excited state spectra (colors) and their fit traces (dotted back) are shown with pump–probe time delays ranging from 1 to 40 ps. Ground state spectra (black) associated with each excited state peak are shown for comparison and scaled for clarity. Left panel: in-plane phenyl deformation mode, ν_{ph} , with ground state frequency 792 cm^{-1} . Middle panel: symmetric quinoidal C=C stretching mode, ν_{CC} , with ground state frequency 1604 cm^{-1} . Right panel: nitrile stretching mode, ν_{CN} , with ground state frequency 2213 cm^{-1} . Difference spectra are offset for clarity.

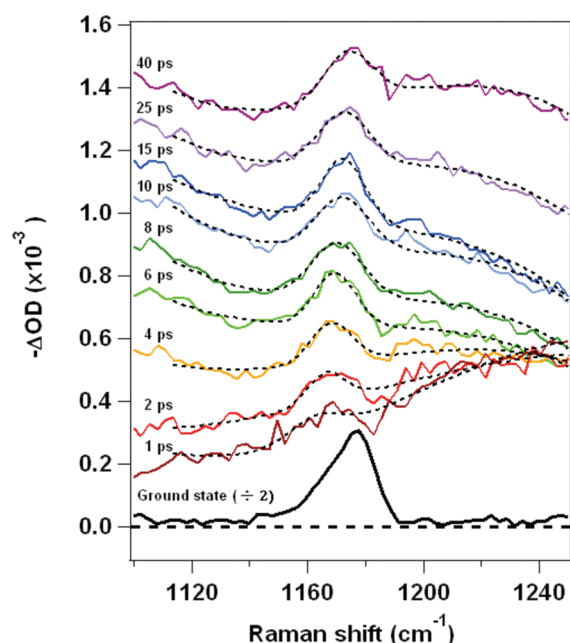


Figure 6. FSR spectra of DMABN in methanol using a 400 nm Raman pump. Pump–probe time delays ranging from 1 to 40 ps (offset for clarity) shown for excited state difference spectra (solid colors) and their fit traces (dotted black) for the in-plane C–H bending mode (δ_{CH}). The fit for the 1 ps trace was omitted from the kinetic analysis due to the poor resolution of peak features. The associated ground-state spectrum (solid black) is scaled and shown for comparison.

frequency of 2213 cm^{-1} . It is initially observed at 2103 cm^{-1} where it remains until between 6 and 7 ps, at which point it shows a down-shift to 2096 cm^{-1} over the next 40 ps (Figure 7a). When fit to an exponential, the down-shift occurs with a time constant of 7.5 ± 2.0 (1σ) ps. (The reported uncertainties are the results from the least-squares fitting algorithms and are reported to one sigma unless otherwise stated.) Also shown in Figure 7a is the simulated spectral shift that would occur if, because of our spectral resolution, the observed ν_{CN} peak was actually the average of the free and HICT peaks observed by Kwok et al. using time-resolved infrared spectroscopy (TRIR), *vide infra*.^{33,35} The ν_{CN} peak area grows in with a 6.4 ± 0.9 ps time constant (Figure 8a), in rough agreement with Kwok's previous measurements using TRIR.^{33,35}

1582 cm^{-1} , ν_{CC} Mode. As reported earlier, the mode at 1604 cm^{-1} in the ground state is assigned to the symmetric quinoidal C=C stretching vibration, ν_{CC} . In the excited state, this peak initially appears at 1573 cm^{-1} at 3 ps and then up-shifts to 1582 cm^{-1} by 40 ps (Figure 7b). This $\sim 10\text{ cm}^{-1}$ shift occurs with a 6.3 ± 0.9 ps time constant, in good agreement with our recently published values for this mode.⁸ The peak area growth was fit to a 5.9 ± 0.6 ps time constant (Figure 8b), which is slightly larger than our recently published results (4.9 ± 0.2) but within 2σ uncertainty. The slight difference may be due to the different kinetics of the growth of the electronic absorption bands at 330 and 400 nm, the two wavelengths responsible for the resonance enhancement of the Raman signal.

1174 cm^{-1} , δ_{CH} Mode. Observed only when using the 400 nm Raman pump (Figure 6), the in-plane CH bending vibration, δ_{CH} , is initially resolvable at 2–3 ps at 1166 cm^{-1} , downshifted relative to its ground state position of 1175 cm^{-1} .

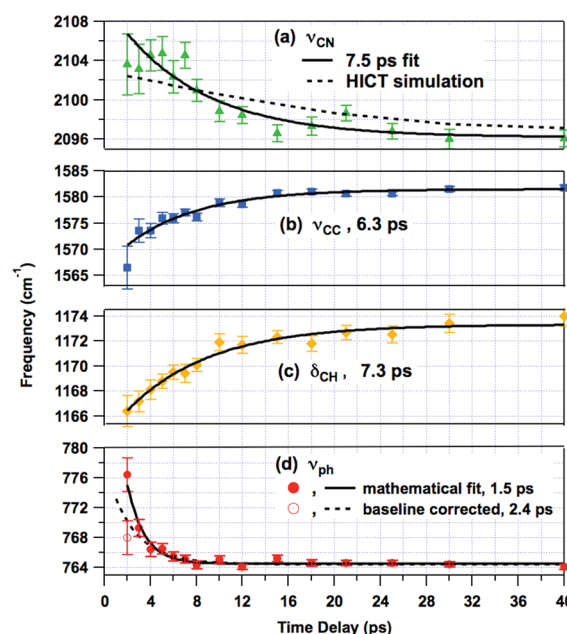


Figure 7. Time dependent frequencies of DMABN's excited state FSR spectrum. Data (colored points) and fits (black lines) are shown for each mode observed in Figures 5 and 6. (a) Nitrile stretch, ν_{CN} , including both an exponential fit (solid line) and a simulation of the spectral shift induced by HICT/free equilibration (see text for details). (b) Quinoidal C=C stretch, ν_{CC} . (c) CH in-plane bend, δ_{CH} . (d) Phenyl ring-breathing mode, ν_{ph} , including data (solid red) and fit (solid black line) from the direct mathematic fit of the peak at 2 ps as well as the baseline corrected peak frequency (open red circle) and the associated exponential fit (dashed black line). (See text for details.)

The subsequent $\sim 8\text{ cm}^{-1}$ shift of this mode by 40 ps to 1174 cm^{-1} occurs with a 7.3 ± 1.8 ps time constant (Figure 7c). Due to the small intensity of the excited state peak, no peak area or width kinetics were determined. Despite this, the peak position values were determined with good accuracy, as seen in the uncertainties associated with each time point.

764 cm^{-1} , ν_{ph} Mode. The excited state in-plane phenyl deformation mode, ν_{ph} , is down-shifted relative to its ground state position of 792 cm^{-1} . The excited state frequency shifts from its initial position of 769 cm^{-1} at 3 ps to a final position of 764 cm^{-1} at 40 ps with a 1.5 ± 0.3 ps time constant (solid line, Figure 7d). This peak is difficult to fit at 2 ps because of a broad feature in the baseline that causes the fit to converge to a very wide peak centered at 776 cm^{-1} . However, inspection of the 2 ps spectrum clearly indicates a small peak centered at 768 cm^{-1} (open circle, Figure 7d). By 3 ps, the peak has grown sufficiently that the mathematical best-fit frequency agrees with the qualitative analysis, centering the peak at 769 cm^{-1} . When the baseline-corrected peak at 768 cm^{-1} at 2 ps is included in the fit, the down-shift in frequency occurs with a 2.4 ± 0.7 ps time constant. Kinetic fitting of the peak area shows a 5.4 ± 0.6 ps growth time constant (Figure 8c).

COMPUTATIONAL RESULTS

Quantum chemical calculations were performed in order to determine the anharmonic vibrational coupling within DMABN's CT state. These calculations can test the hypothesis that the time-dependent frequency shifts in Figure 7 can be attributed to vibrational relaxation of a subset of CT receiving modes. However, because a complete mapping of the CT state

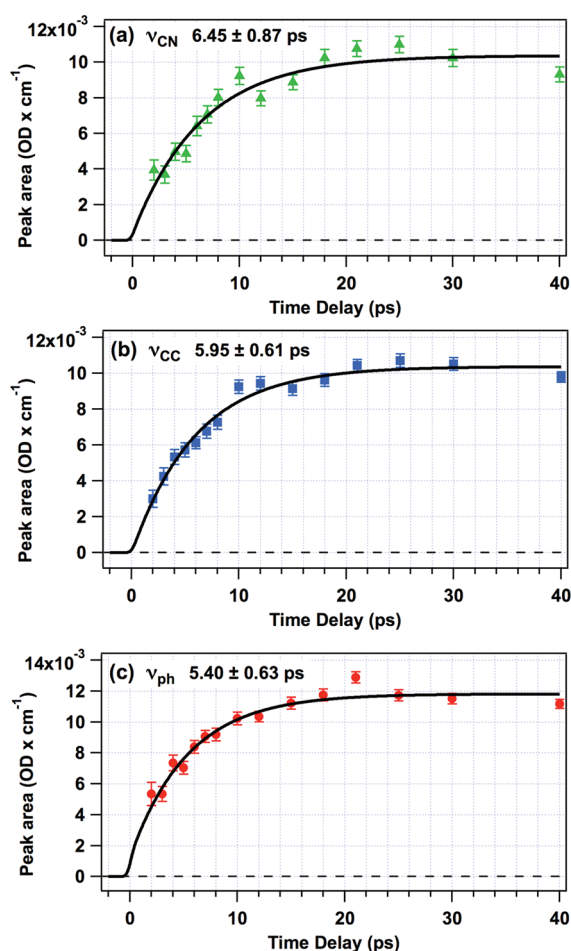


Figure 8. Peak area kinetics shown for each excited state FSRS mode observed in Figure 5: (a) nitrile stretch (ν_{CN}); (b) symmetric quinoidal C=C stretch (ν_{CC}); (c) phenyl deformation (ν_{ph}). Time constants and uncertainties for each exponential fit are shown in each corresponding figure.

vibrational potential would be exceedingly difficult, we chose to model the anharmonicity using the radical anion, whose vibrational spectrum matches that of the dominant modes of DMABN's CT state. Because the anion is an open shell *ground-state* compound, the calculations are accelerated significantly. In previous work, we used calculations of the benzonitrile radical anion, $\text{BZN}^{\bullet-}$, to model the anharmonicity of DMABN's CT state. Using the benzonitrile radical anion as a molecular analogue to DMABN is justified on the basis of the decoupled nature of the benzonitrile group from the dimethylamino group in the CT state and also because of the strong similarity between the vibrational spectrum of $\text{BZN}^{\bullet-}$ and that of DMABN's CT state.^{8,17,19,34} In this work, we used four different model compounds, shown in Figure 9, that

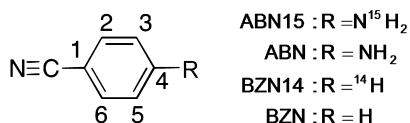


Figure 9. Series of molecules used to model the CT state vibrational spectrum of DMABN in the presented computational investigations.

include BZN and three new models designed to include the effects of a heavy atom substituent in the 4-position. The group

at the para-position was varied from H (BZN) to ^{14}H (BZN14) to NH_2 (ABN) and then N^{15}H_2 (ABN15). The mass 14 hydrogen benzonitrile, BZN14, was used to investigate the importance of heavy atom substitution at the para position relative to the nitrile. In the amino-benzonitrile model, ABN, the para-hydrogen was replaced with an $-\text{NH}_2$ group. The ABN analogue is the simplest molecular model that could simulate vibrational coupling between the phenyl and a twisted amine. The ABN15 model, with mass 15 hydrogens on the amine, was used to simulate the mass of the methyl groups within the twisted amine. $\text{ABN15}^{\bullet-}$ was hypothesized to be the best model for the kinetic coupling of internal coordinates in the CT state without the added complications introduced by internal rotations of methyl groups. Calculations for each molecule were performed on the radical anion form of the ground electronic state to model the CT state and then the neutral ground electronic state for comparison. Using any basis set, the ABN15 model consistently improved the accuracy of the calculation. For instance, at the 6-31G(d) level, the rms frequency deviation decreased from 35 cm^{-1} for the $\text{BZN}^{\bullet-}$ compound to 28 cm^{-1} for the $\text{ABN15}^{\bullet-}$ compound (see Table 1). Between BZN, BZN14, ABN, and ABN15, we

Table 1. Comparison of Computational and Experimental Vibrational Frequencies

compound	DFT basis set	vibrational frequency ^b (cm^{-1})				rms difference (cm^{-1})
		ν_{CN}	ν_{CC}	δ_{CH}	ν_{ph}	
DMABN	experimental	2096	1582	1174	764	
ABN15 (radical anion)	6-31G(d)	2150	1595	1168	771	28.2
	6-31G(d,p)	2148	1588	1163	769	26.9
	6-31+G(d,p)	2122	1555	1158	770	20.6
	6-311+G(d,p)	2120	1545	1148	768	25.7
BZN (radical anion)	6-31G(d) ^a	2146	1604	1181	721	34.9
	6-31G(d,p)	2149	1601	1175	722	35.1
	6-31+G(d,p)	2122	1573	1169	732	21.2
	6-311+G(d,p)	2121	1557	1166	724	27.0

^aPreviously published results.⁸ ^bComputed frequencies are unscaled fundamental frequencies incorporating the effects of anharmonicity.

observed little convergence in the anharmonic coupling matrix. This indicated that the anharmonic coupling of the benzene ring depended critically on appropriate mass substituents at the para (C_4) position. Hence, all detailed analysis presented herein is of the ABN15 model compound.

Using DFT with B3LYP functionals, we tested a series of basis sets to determine the most accurate when using the anion as a model of DMABN's CT state. The eight basis sets used were 6-31G(d), 6-31G(d,p), 6-31+G(d,p), 6-311+G(d,p), 6-31++G(d), 6-31++G(d,p), 6-311++G(d), and 6-311++G(d,p). Basis sets that included diffuse orbitals for the hydrogen atoms (++ notation) produced a physically unreasonable negative charge that was localized on the hydrogen atoms of the benzene ring, and also inverted the molecular dipole such that the negative pole resided on the amine side and the positive pole toward the nitrile. The four remaining basis sets produced reasonable directions of the dipole and an appropriately planar amine in the ground state and twisted amine in the anionic state. These basis sets were further assessed on the basis of the accuracy with which they reproduced the CT state vibrational

frequencies (Table 1). The 6-31+G(d,p) basis set was found to improve the accuracy significantly, reducing the rms deviation of the vibrational frequencies to 20.6 cm⁻¹.

As shown in Table 2, using the B3LYP/6-31+G(d,p) method, the ABN15 model reproduces all the important structural

Table 2. Structural Comparison of ABN15^{•-}, BZN^{•-}, and the CT State of DMABN

	ABN15 ^a		BZN ^{•-}		DMABN CT state		
	neutral	rad. anion	ref 8	ref 12	ref 11	ref 10	ref 13
R ₁₂	1.408	1.454	1.451	1.422	1.433	1.427	1.438
R ₂₃	1.388	1.383	1.377	1.370	1.375	1.369	1.373
R ₃₄	1.410	1.417	1.422	1.445	1.433	1.441	1.430
R _{1C}	1.431	1.398	1.397	1.393	1.422	1.425	1.405
R _{CN}	1.165	1.186	1.185	1.174	1.187	1.165	1.192
R _{4N}	1.384	1.448		1.431	1.453	1.452	1.420

^aABN15 results are from B3LYP/6-31+G(d,p) calculations in this work.

characteristics of both the ground state and CT state of DMABN. This includes a switch from a benzenoid ground state with nearly equivalent ring bond lengths to a quinoidal anion state in which R_{2,3} is significantly shorter than R_{1,2} and R_{3,4}. Additionally, the model anion reproduces the lengthening R_{4,N} bond that has been observed in previous computational work and is inferred by the decrease in frequency of the ph-N vibration in the CT state.^{10–13,19} This change is accompanied by the previously mentioned twist of the amine from a planar neutral species to a perpendicular orientation in the anion.

Results of the anharmonic vibrational calculation on ABN15^(•-) using B3LYP methodology with a basis set of 6-31+G(d,p) can be seen in Table 3 and Figure 10. Harmonic frequencies and fundamental transition frequencies are reported, in addition to the χ_{ij} anharmonic coupling constants between all 39 (=3N – 6) modes and the four experimentally observed modes. Atomic displacement diagrams of each normal mode are given in the Supporting Information. The anharmonic coupling shifts each vibrational energy according to

$$E_v = E_0 + \sum_{i=1}^{3N-6} \omega_i \left(v_i + \frac{1}{2} \right) + \sum_{i=1}^{3N-6} \sum_{j \leq i} \chi_{ij} \left(v_i + \frac{1}{2} \right) \left(v_j + \frac{1}{2} \right) \quad (2)$$

in which v_i is the vibrational quantum number of mode i , ω_i is the harmonic frequency of mode i , and χ_{ij} is the anharmonic coupling between modes i and j .^{52,58} The anharmonicity produces a frequency of the $\Delta v_j = +1$ transition, i.e., the $(v_i, v_j = 0) \rightarrow (v_i, v_j = 1)$ transition, of

$$\begin{aligned} \omega_{v_i, v_j=0} &= \Delta E((v_i, v_j = 0) \rightarrow (v_i, v_j = 1)) \\ &= \omega_j + 2\chi_{j,j} + \frac{1}{2} \sum_{k \neq j} \chi_{k,j} + \chi_{i,j} v_i \end{aligned} \quad (3)$$

In this way, vibrational excitation in mode i will shift the observed $v_j = 0 \rightarrow 1$ transition of mode j away from its fundamental frequency. When $v_i = 0$, eq 3 reduces to give the fundamental frequency of mode j .

Comparing the calculated normal-mode frequencies and qualitative assignments, the observed modes can be assigned as follows: ν_{ph} (764 cm⁻¹) corresponds to calculated mode #19,

the ring breathing mode; δ_{CH} (1174 cm⁻¹) corresponds to calculated mode #25, the phenyl C—H bending mode; ν_{CC} (1582 cm⁻¹) corresponds to calculated mode #34, the symmetric quinoidal C=C stretch; and ν_{CN} (2096 cm⁻¹) corresponds to calculated mode #35, the CN stretch. Anharmonic shifts caused by the χ_{ij} couplings, i.e., the spectral shift of the $\Delta v_j = +1$ transition caused by mode i being in the $v_i = 1$ excited state, are displayed in Table 3. Couplings of all 3N – 6 modes to the four observed vibrations are shown in Figure 10. For comparison, Figure 10 also shows dashed lines to indicate the observed frequency shift of each vibration between 2 and 40 ps from the data shown in Figure 7. For instance, the horizontal dashed line in Figure 10c indicates that the frequency of the ν_{CC} mode up-shifts by ~11 cm⁻¹ between 2 and 40 ps.

The lowest computed frequency (Table 3) was slightly negative (–21 cm⁻¹), indicating a lack of structural convergence along the ph-NH₂ twist coordinate. However, this is expected from previous high-level excited state calculations that established that the potential is nearly flat along this coordinate.⁹ Interestingly, the fundamental frequency of this mode is positive (+29 cm⁻¹), indicating that, when anharmonicity is included, higher order terms in the potential may enforce a bound potential energy surface as the mode distorts from the slight saddle-point to which the geometry converged.

DISCUSSION

The global analysis of the TA kinetics establishes the presence of dynamics occurring on three time scales: 0.3, 2, and 6 ps. In the 0.3 ps DAS (red, Figure 4), it is apparent that on this time scale there is a broad loss of TA signal from 380 to 440 nm and a slight growth of the LE TA band from 530 to 620 nm. Though it is difficult to assign this signal because of our limited time resolution, we feel that this fast relaxation could correspond to the relaxation from the Franck–Condon surface in the optically active L_a state to the lower lying L_b or “LE” state. Such an ultrafast relaxation process is hypothesized because of the close proximity of these states established in previous theoretical work,^{10,11,25} in particular Gomez’s work that established a conical intersection seam that can funnel population efficiently into the LE state.¹⁰ However, it is also possible that this signal corresponds to rapid vibrational relaxation on the L_a state surface, with DMABN staying in the same electronic state to which it was excited by the 266 nm pump pulse. While these data do not allow us to distinguish between these processes, most fluorescence and theoretical work in the field is consistent with the rapid population of a lower L_b (LE) electronic state following excitation to the L_a Franck–Condon region.

The DAS for the 2–2.4 ps time constant (green, Figure 4) corresponds to the complete loss of the broad LE TA signal from 480 to 620 nm, the growth of a broad absorption band from 360 to 425 nm, and the growth of the sharp absorption band from 320 to 350 nm. The 6 ps DAS (blue, Figure 4) includes almost no amplitude from 440 to 620 nm but a distinctive growth and narrowing of the 380–425 nm ICT absorption band and a dramatic growth of the absorption band from 300 to 320 nm. Spectral narrowing is a stereotypical signature of excited state vibrational relaxation. All of these are consistent with the conversion of the LE state population to a vibrationally hot ICT state with a 2 ps time constant and subsequent vibrational relaxation within the ICT state in 6 ps.

We attribute the discrepancy between the 2 ps rate of LE decay and the 6 ps rate of relaxed TICT appearance to the formation of an intermediate vibrationally hot CT* state, but

Table 3. Computed Vibrational Frequencies and Anharmonicities of the Aminobenzonitrile Radical Anion (ABN15^{•-})^a

normal mode	unscaled harmonic frequency, ω_i	fundamental frequency, $\omega_{0,0}$	$\chi_{i,19}$ anharmonic coupling to ν_{ph}	$\chi_{i,25}$ anharmonic coupling to δ_{CH}	$\chi_{i,34}$ anharmonic coupling to ν_{CC}	$\chi_{i,35}$ anharmonic coupling to ν_{CN}	qualitative assignment ^b
1	−21	29	2.08	10.49	−0.33	−1.45	φ ph-N*
2	70	69	−0.09	0.44	−0.11	0.08	sym. oop ph-N + δ_{CN}
3	96	233	0.25	6.37	−1.97	−1.03	oop C ₁ −C ₄ + CN bend, ψ N ¹⁵ H ₂
4	137	138	0.14	0.21	1.80	−0.76	sym. ip $\delta_{\text{ph-N}} + \delta_{\text{CN}}$
5	218	217	0.39	−0.03	0.01	−0.29	asym. ip ψ N ¹⁵ H ₂ + δ_{CN}
6	239	267	1.30	3.47	−1.46	−0.53	oop C ₁ −C ₂ −C ₃ −C ₅ −C ₆ − δ_{CN}
7	328	326	−0.32	0.08	−0.83	−0.06	asym. ring br., ph def
8	426	441	−0.84	0.87	−0.99	−0.37	asym. oop ψ N ¹⁵ H ₂ + ph def
9	444	438	−1.00	−0.62	−2.22	−0.85	asym. oop ph def
10	477	482	−1.27	2.46	−0.24	−7.77	sym. oop ph def − oop δ_{CN}
11	485	477	−3.54	−0.37	−0.55	−0.23	asym. ph def, $\delta_{\text{ph-N}}$ *
12	505	500	−0.67	−0.11	−0.27	−0.13	ip ph def, $\beta_{\text{ph-N}}$ *
13	559	557	0.79	4.54	−11.64	−4.13	ip δ_{CN}
14	632	626	−0.55	−0.49	−2.26	−0.07	oop C ₁ + C ₃ + C ₅ −C ₂ −C ₄ −C ₆
15	650	643	0.15	−0.73	−2.06	−0.47	ip ph def
16	689	688	−1.32	−2.33	−1.88	0.37	sym. oop $\delta_{\text{C-H}}$
17	698	681	−1.00	−1.16	−2.77	−0.86	ip ph def, $\beta_{\text{ph-N}} - \nu_{\text{C-CN}}$ *
18	734	713	−0.16	−4.37	−4.84	0.45	asym. oop $\delta_{\text{C-H}}$
19 ^c	779	771	−1.11	−0.68	−0.31	0.83	ring br.
20	898	864	−0.29	−5.91	−4.93	0.14	asym. oop $\delta_{\text{C-H}}$
21	917	883	−0.37	−5.27	−1.31	0.32	asym. oop $\delta_{\text{C-H}}$
22	973	960	−0.96	−1.53	−4.18	0.20	ip $\nu_{12} + \nu_{16} - \nu_{34} - \nu_{45}$
23	1090	1065	−0.63	−0.88	−2.22	−0.05	ip ph def, $\nu_{\text{N-H}}$
24	1103	1091	−0.53	2.40	−11.81	−0.66	ip C ₁ , asym. $\delta_{\text{C-H}}$
25 ^c	1174	1158	−0.68	−0.39	−20.12	−1.92	ip C ₄ , sym. $\delta_{\text{C-H}}$
26	1195	1173	−1.00	7.95	−15.16	−1.08	ip $\delta_{\text{C-H}}$, $\nu_{12} + \nu_{45} - \nu_{34} - \nu_{16}$
27	1242	1217	−1.74	−1.95	−4.30	−5.42	sym. ip $\delta_{\text{C-H}}$ ph def, $\nu_{\text{C-CN}}$
28	1291	1252	−0.48	−1.50	−2.85	−0.30	ip $\nu_{12} + \nu_{34} - \nu_{45} - \nu_{56} - \nu_{\text{ph-N}}$
29	1305	1270	−1.76	−1.22	−2.84	−0.59	ip $\nu_{12} + \nu_{34} + \nu_{\text{ph-N}} - \nu_{45} - \nu_{56}$
30	1350	1337	−0.05	0.31	−0.41	−0.04	asym. $\nu_{\text{N-H}}$ *
31	1361	1337	−0.74	−0.27	−20.02	−0.32	ph def, ip asym. $\delta_{\text{C-H}}$
32	1473	1439	−0.53	−4.9	−13.82	−0.47	ip $\nu_{23} - \nu_{56}$
33	1482	1446	−1.25	−3.35	−6.93	−1.72	ip $\delta_{\text{C-H}}$, $\nu_{12} + \nu_{16} - \nu_{34} - \nu_{45}$
34 ^c	1627	1555	−0.31	−20.12	−2.14	−1.98	ip $\nu_{23} + \nu_{56}$
35 ^c	2160	2122	0.83	−1.92	−1.98	−23.36	ip ν_{CN}
36	3120	2996	−0.01	−1.53	4.711	0.10	asym. ip $\nu_{\text{C-H}}$
37	3149	3029	−0.24	−2.51	2.55	0.25	asym. ip $\nu_{\text{C-H}}$
38	3166	3036	−0.29	−6.23	−2.71	0.70	sym. ip $\nu_{\text{C-H}}$
39	3177	3038	−0.22	−0.96	1.25	0.55	sym. ip $\nu_{\text{C-H}}$

^aAll frequencies in cm^{−1}. ^bMode abbreviations: ip = in plane, oop = out of plane, br = breathing, ph def = phenyl deformation, $\nu_{\text{a-b}}$ = stretch of a–b bond, δ = bend, $\varphi_{\text{a-b}}$ = twist of a–b bond, ψ = rock, β = scissor, “+” and “−” indicate relative internal coordinate motion, sym. = symmetric, asym. = asymmetric. The “*” indicates normal modes whose internal coordinate motions are likely to be distorted by the substitution of ¹⁵H for methyl groups in the ABN15^{•-} model. ^cModes observed in this work.

these kinetics could also be interpreted as support for the presence of an intermediate $\pi\sigma^*$ (aka RICT state).²¹ However, given the significant solvent reorganization necessary to stabilize the $\pi\sigma^*$ state, we feel that it is unlikely that it could be formed on the 0.3 ps time scale. Lim and co-workers have assigned the 620–700 nm TA band to a $\pi\sigma^*$ electronic state using TDDFT, and thereby hypothesized that the $\pi\sigma^*$ state is a precursor to the final ICT state.^{21,26} CASSCF/CASPT2 calculations by Lim and co-workers and RASSCF/CASPT2 calculations by Robb and co-workers have determined that the $\pi\sigma^*$ state is 1–1.4 eV above the LE state in vacuum but that its large dipole moment (13–17 D in vacuum, 22 D in acetonitrile) allows it to drop in energy in a polar solvent.^{10,25} However, in order to realize the stability of the $\pi\sigma^*$ state in solution, complete dielectric relaxation of the solvent would be required. It is unlikely that solvent reorganization could occur

sufficiently fast that the $\pi\sigma^*$ state would be stabilized in 0.3 ps, allowing it to be populated by the L_a state. In particular, solvents such as acetonitrile and methanol have small high-frequency dielectrics (i.e., small refractive indexes) and hence require significant reorientation on the picosecond time scale to realize their full dielectric response.^{59,60} Hence, we feel that our signal is consistent with the dominant paradigm in the field in which the initially populated L_a state relaxes to the LE (L_b) state in ~0.3 ps, which subsequently relaxes to the TICT state in 2 ps. The L_a–LE relaxation does not require dramatic solvent reorganization and can proceed on the <1 ps time scale. The TICT state is also stabilized by the dielectric reorganization of the solvent, but only a small dielectric fluctuation is required to bring it into resonance with the LE state, since it lies only slightly higher in energy in vacuum.^{10,11,25} Clearly, more experiments are necessary to definitively establish the state-by-state

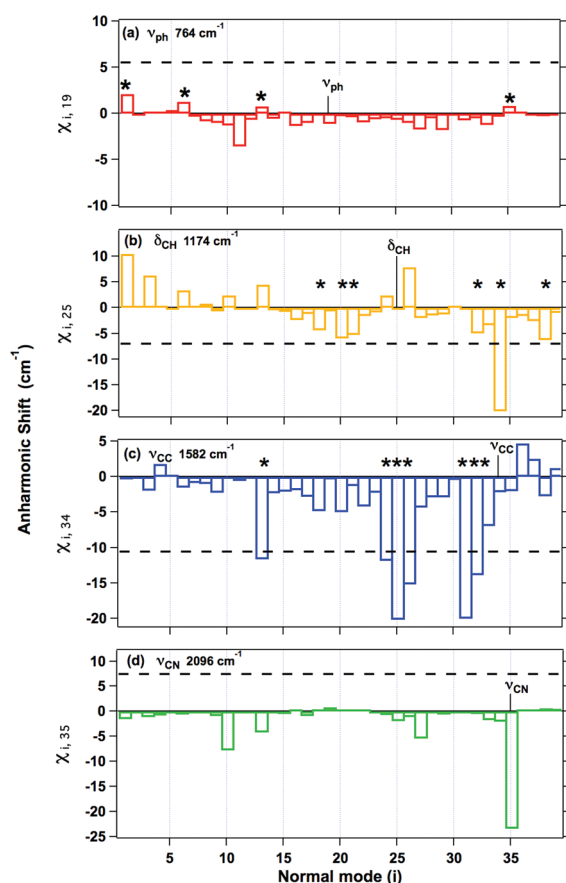


Figure 10. Anharmonic shifts, $\chi_{i,j}$ of each vibrational mode, i , of ABN15^(•-) to the four experimentally observed vibrations, $j = 19, 25, 34$, and 35 : (a) coupling to mode #19, the phenyl ring-breathing mode, ν_{ph} , observed at 764 cm^{-1} ; (b) coupling to mode #25, the phenyl C—H bending vibration, δ_{CH} , observed at 1174 cm^{-1} ; (c) coupling to mode #34, the quinoidal C=C stretch, ν_{CC} , observed at 1582 cm^{-1} ; (d) coupling to mode #35, the nitrile stretch, ν_{CN} , observed at 2096 cm^{-1} . Dashed lines indicate the shift in frequency of the vibration occurring between 2 and 40 ps, $\omega(2 \text{ ps}) - \omega(40 \text{ ps})$.

relaxation mechanism from the Franck–Condon surface to the bottom of the TICT electronic state potential.

The discrepancy in the LE decay and CT growth in the TA data agrees with our previous results. It is also indicative of the two-dimensional model put forth by Kim and Hynes^{59–61} and supported by Changenet et al.⁶² Their calculations indicated that in methanol the reaction coordinate is initiated by inner-sphere motion along the amine-twisting coordinate. Subsequent solvent reorganization brings the system to the transition state. Once the system crosses over into the CT state potential, relaxation is dominated by additional inner-sphere reorganization, i.e., amine twisting and small additional solvent reorganization. Though the Hynes model lacks structural details beyond the amine twist, it generally agrees with our observation that the $\sim 6 \text{ ps}$ time scale dynamics involve a significant amount of inner-sphere reorganization and not just solvent reorganization.

The time-resolved FSRS spectra can provide a more detailed picture of the ICT mechanism by providing probes of mode-specific dynamics. In our previous work, we showed that the spectral changes could not be explained by a dynamic Stark effect induced by the reaction field of the solvent reorganization.⁸ Instead, we attributed the dramatic downshift of ν_{CC} at 2 ps to off-diagonal anharmonic coupling with either the

asymmetric quinoidal vibration, corresponding to mode #32 in these calculations, or the NC-ph bending vibration, mode #13 here. We hypothesized that mode #32 (which was #26 in the original work) could receive significant excitation in the ICT process because of its significant projection onto one of the degeneracy lifting coordinates determined by Gomez.¹⁰ Similarly, the NC-ph bending vibration (#13 here or #8 in the original work) would be significantly excited if the molecule passed through the $\pi\sigma^*$ electronic state, characterized by a bent NC-ph angle. Our improved calculations using the ABN15^(•-) model compound with a 6-31+G(d,p) basis confirm our original analysis. In Figure 10c, both mode #13 and mode #32 show strong anharmonic coupling to ν_{CC} that is sufficient that a one- or two-quantum excitation in either mode could induce the $10\text{--}12 \text{ cm}^{-1}$ downshift observed in ν_{CC} at early times.

Unfortunately, the observation of the relaxation dynamics of three other modes, in addition to ν_{CC} , does not clarify exactly what are the receiving modes of the ICT process, i.e., which modes are strongly coupled to CT. Inspecting Figure 10, it is clear that there is no simple set of modes that, if excited at early times, would simultaneously explain the frequency shifts of all four observed modes. Instead, our data indicate that each vibrational mode is reacting to different aspects of the ICT mechanism, thereby illuminating the complicated nuclear dynamics accompanying the CT.

The integrated areas of the ν_{ph} , ν_{CC} , and ν_{CN} peaks all grow in with similar time constants of $\sim 6 \text{ ps}$. The coincidence of this time constant with the vibrational relaxation time constant observed in the global fitting of the TA kinetics indicates that the growth of the FSRS signal in the CT state is limited by the vibrational relaxation process. This is consistent with other picosecond time-resolved Raman experiments that have seen decreased signal from vibrationally hot species, a consequence of the loss of resonance Raman enhancement.⁶³

The ν_{ph} mode experiences much more rapid spectral relaxation than the other modes, down-shifting from 768 to 764 cm^{-1} with a $\sim 2 \text{ ps}$ time constant. Since this mode has negligible diagonal anharmonicity, $\chi_{19,19}$ in Table 2 and Figure 10, the spectral shift cannot be accounted for by simple vibrational relaxation within the ν_{ph} manifold. Additionally, Figure 10 indicates that there are no other vibrational modes whose excitation and subsequent relaxation could account for the 4 cm^{-1} upshift. Modes 6, 13, and 35 all have slightly positive anharmonicities, but their small magnitudes indicate that they would need to be in $\nu_i > 4$ to induce the observed shift. It is unlikely that any mode would be so highly excited by the CT process, though it is possible for a low frequency mode such as #6. Having excluded vibrational anharmonicity as a mechanism for the upshift, the only possibility is that there are structural changes occurring on the 2 ps time scale that decrease the ring-breathing restoring force slightly. Torsion of the amine and pyramidalization of C_4 (Figure 9) both could contribute to the rapid decrease in frequency of ν_{ph} , and are important structural changes predicted to be involved in the CT reaction coordinate.^{10,11,25} Hence, it appears that significant structural changes may occur very rapidly once DMABN converts from the LE state to the hot ICT state surface.

The C—H bending vibration, δ_{CH} , and the quinoidal C=C stretch, ν_{CC} , both experience a spectral upshift with $6\text{--}7 \text{ ps}$ time constants (Figure 7). This is the standard signature of vibrational relaxation, but the negligible diagonal anharmonicity of each mode, $\chi_{25,25}$ and $\chi_{34,34}$, indicates that the decreased frequencies observed at early times must be due to excitation

residing in other modes that are strongly coupled to δ_{CH} and ν_{CC} via off-diagonal anharmonicity. As shown in Figure 10, there are a variety of modes that have significant negative anharmonic coupling to δ_{CH} and ν_{CC} . Eliminating the out-of-plane vibrations, for which there is little driving force for excitation during ICT, the remaining strongly coupled modes are the CN-bend (#13, 559 cm^{-1}), various CH-bending vibrations (#24–27, 1100–1250 cm^{-1}), and the symmetric and antisymmetric quinoidal C=C vibrations that are mixed with CH bends (#31–34, 1350–1550 cm^{-1}). Initial excitation of the quinoidal C=C vibrations could explain the down-shift of δ_{CH} and ν_{CC} at early times. However, no single mode stands out, especially considering that the large positive anharmonicities of the CN- and CH-bending vibrations to δ_{CH} could be balanced by excitation of ν_{CC} , which has strong negative anharmonicity to δ_{CH} . Hence, the observed spectral shift may be the combined effect of the excitation of several different receiving modes. The CN bend (#13), CH bends (#24–27), and the C–C and C=C stretches (#31–34) are the most likely receiving modes that could be vibrationally excited at 2 ps.

The down-shift of the nitrile stretching, ν_{CN} , frequency with time is very uncharacteristic for simple vibrational relaxation processes, especially considering that there is no mode that has significant positive anharmonicity to ν_{CN} (Figure 10c). However, the down-shift is consistent with the presence of a hydrogen-bonded species in the CT state. Time-resolved infrared (TRIR) work by Kwok et al. observed the effect of hydrogen bonding on the nitrile frequency.^{33,35} In protic solvents such as methanol, the nitrile peak was resolved into two components: a higher frequency peak at 2109 cm^{-1} that grows in first and a down-shifted peak at 2091 cm^{-1} that grows in more slowly and establishes an equilibrium with the first peak. Kwok observed that the total intensity of the nitrile grows in with a 5.5 ps time constant, in agreement with the kinetics of the ν_{CN} FSRs signal. Because of our limited spectral resolution, it is likely that we are observing a gradual down-shift of unresolved doublet peaks instead of a down-shifted peak growing in at the expense of the higher frequency peak, as Kwok did. In Figure 7a, we show both a direct exponential fit to the spectral shift of the nitrile peak (solid line) and a simulation of what Kwok's spectra would look like if observed with our spectral resolution and fit to a single peak (dashed line). In the TRIR experiments, the down-shifted peak grew in with a 13 ps time constant, which results in the average frequency of the two modes (dashed line in Figure 7a) decreasing with roughly an ~ 22 ps time constant, significantly slower than the observed 7.5 ps shift of ν_{CN} in our FSRs data. Despite this discrepancy, the qualitative agreement between the dashed curve and the spectral shift of ν_{CN} allows us to conclude that we are observing the same fundamental equilibration as was observed in Kwok's TRIR work. However, as discussed below, it is likely that the assignment of the two nitrile peaks in the TRIR data was incorrect.

Extensive investigation into the spectroscopic shifts of nitrile vibrations has established that the nitrile frequency is primarily influenced by its position on the aromatic ring and electron donating character of the ring.^{64–70} More recent studies by Zhao and Han dealing specifically with DMABN have given a possible reassignment of the HICT and “free” nitrile frequencies previously assigned by Kwok.⁷¹ Using DFT calculations, Zhao and Han showed that hydrogen bonding to the nitrile actually up-shifts the nitrile frequency in DMABN. This is in contrast to the usual picture of hydrogen-bonding-induced downshifts attributed to a softening of the stretching potential but consistent

with other studies of hydrogen bonding to nitriles.^{72,73} Kwok observed an initially populated vibrational mode at 2109 cm^{-1} that was then red-shifted at longer pump–probe delay times. On the basis of the work of Zhao and Han, it is likely that the initially appearing mode can be assigned to that of the HICT state, which then experiences a down-shift as hydrogen-bonding character is lost in the CT state. It follows then that the spectral shift we observe is caused by the disappearance of the HICT state and growth of the “free” state, forcing the average peak position of the unresolved doublet to gradually downshift.

CONCLUSION

Time-dependent changes in TA and Raman spectra were recorded for DMABN in methanol in the range of 0–40 ps, revealing a dynamic picture of the CT state formation. Global analysis of the TA kinetics from 280 to 600 nm allows us to establish three primary processes that lead to the relaxed CT state: (1) initial relaxation from the L_a Franck–Condon state to the nearby L_b (LE) state occurs in ~ 0.3 ps; (2) the LE state disappears with a 2 ps time constant, forming a highly vibrational excited CT state species; (3) the hot CT state relaxes primarily by intramolecular vibrational relaxation with an ~ 6 ps time constant. Observation of four excited state vibrational modes—the phenyl/ring breathing at 764 cm^{-1} , CH in-plane bend at 1174 cm^{-1} , quinoidal C=C stretch at 1582 cm^{-1} , and nitrile stretch at 2096 cm^{-1} —has allowed for a more complete picture of the complicated multidimensional dynamics that accompany the charge transfer. In conjunction with anharmonic vibrational calculations of the ABN^(•−) model compound, we attribute the spectral shifts of each vibrational mode to different processes. The ring-breathing mode at 764 cm^{-1} , ν_{ph} , experiences a rapid upshift in frequency in 2 ps which is likely due to rapid structural changes, primarily C_4 -pyramidalization and amine twisting, that occur shortly after the molecule arrives on the CT state surface. The CH-bending vibration at 1174 cm^{-1} , δ_{CH} , and the quinoidal C=C stretch at 1582 cm^{-1} , ν_{CC} , are initially downshifted by off-diagonal anharmonic coupling to several possible receiving modes. Vibrational relaxation of the receiving modes in ~ 6 ps causes the spectral upshift of δ_{CH} and ν_{CC} . Finally, over the first 15 ps, the nitrile stretching vibration, ν_{CN} , down-shifts from its initial frequency, indicative of the equilibration between a hydrogen-bonded and free species in solution. As is typical with most studies of DMABN over the past 50 years, this data invites further experimental and theoretical studies into the microscopic mechanism of the CT process.

ASSOCIATED CONTENT

Supporting Information

Table showing computed vibrational frequencies and anharmonicities of the aminobenzonitrile radical anion and figures showing normal mode diagrams for ABN15^(−). This material is available free of charge via the Internet at <http://pubs.acs.org>.

AUTHOR INFORMATION

Corresponding Author

*E-mail: mccamant@chem.rochester.edu.

Notes

The authors declare no competing financial interest.

■ ACKNOWLEDGMENTS

This work was supported by a Knowledge Build Grant from ExxonMobil Research and Engineering Company and by a Sloan Foundation Research Fellowship to DWM. Acknowledgment is made to the donors of The American Chemical Society Petroleum Research Fund for partial support of this work.

■ REFERENCES

- (1) Lippert, E. *Angew. Chem.* **1961**, *73*, 695–706.
- (2) Lippert, E.; Rettig, W.; Bonacic-koutecky, V.; Heisel, F.; Miehle, J. A. *Adv. Chem. Phys.* **1987**, *68*, 1–173.
- (3) Grabowski, Z. R.; Rotkiewicz, K.; Rettig, W. *Chem. Rev.* **2003**, *103*, 3899–4031.
- (4) Rettig, W. *Angew. Chem., Int. Ed.* **1986**, *25*, 971–988.
- (5) Hättig, C.; Hellweg, A.; Köhn, A. *J. Am. Chem. Soc.* **2006**, *128*, 15672–15682.
- (6) Yoshihara, T.; Galievsky, V. A.; Druzhinin, S. I.; Saha, S.; Zachariasse, K. A. *Photochem. Photobiol. Sci.* **2003**, *2*, 342–353.
- (7) Dahl, K.; Biswas, R.; Ito, N.; Maroncelli, M. *J. Phys. Chem. B* **2005**, *109*, 1563–1585.
- (8) Rhinehart, J. M.; Mehlenbacher, R. D.; McCamant, D. *J. Phys. Chem. B* **2010**, *114*, 14646–14656.
- (9) Rappoport, D.; Furche, F. *J. Am. Chem. Soc.* **2004**, *126*, 1277–1284.
- (10) Gomez, I.; Reguero, M.; Boggio-Pasqua, M.; Robb, M. A. *J. Am. Chem. Soc.* **2005**, *127*, 7119–7129.
- (11) Cogan, S.; Zilberg, S.; Haas, Y. *J. Am. Chem. Soc.* **2006**, *128*, 3335–3345.
- (12) Scalmani, G.; Frisch, M. J.; Mennucci, B.; Tomasi, J.; Cammi, R.; Barone, V. *J. Chem. Phys.* **2006**, *124*, 094107–15.
- (13) Kohn, A.; Hättig, C. *J. Am. Chem. Soc.* **2004**, *126*, 7399–7410.
- (14) Ma, C.; Kwok, W. M.; Matousek, P.; Parker, A. W.; Phillips, D.; Toner, W. T.; Towrie, M. *J. Photochem. Photobiol. A* **2001**, *142*, 177–185.
- (15) Ma, C.; Kwok, W. M.; Matousek, P.; Parker, A. W.; Phillips, D.; Toner, W. T.; Towrie, M. *J. Phys. Chem. A* **2002**, *106*, 3294–3305.
- (16) Okamoto, H.; Inishi, H.; Nakamura, Y.; Kohtani, S.; Nakagaki, R. *J. Phys. Chem. A* **2001**, *105*, 4182–4188.
- (17) Okamoto, H.; Kinoshita, M. *J. Phys. Chem. A* **2002**, *106*, 3485–3490.
- (18) Rappoport, D.; Furche, F. *J. Am. Chem. Soc.* **2004**, *126*, 1277–1284.
- (19) Kwok, W. M.; Ma, C.; Matousek, P.; Parker, A. W.; Phillips, D.; Toner, W. T.; Towrie, M.; Umapathy, S. *J. Phys. Chem. A* **2001**, *105*, 984–990.
- (20) Zgierski, M. Z.; Lim, E. C. *J. Chem. Phys.* **2005**, *122*, 111103.
- (21) Lee, J. K.; Fujiwara, T.; Kofron, W. G.; Zgierski, M. Z.; Lim, E. C. *J. Chem. Phys.* **2008**, *128*, 164512.
- (22) Gustavsson, T.; Coto, P. B.; Serrano-Andres, L.; Fujiwara, T.; Lim, E. C. *J. Chem. Phys.* **2009**, *131*, 031101–4.
- (23) Galvan, I. F.; Martin, M. E.; Aguilar, M. A. *Chem. Phys. Lett.* **2010**, *499*, 100–102.
- (24) Zgierski, M. Z.; Fujiwara, T.; Lim, E. C. *Acc. Chem. Res.* **2010**, *43*, 506–517.
- (25) Coto, P. B.; Serrano-Andres, L.; Gustavsson, T.; Fujiwara, T.; Lim, E. C. *Phys. Chem. Chem. Phys.* **2011**, *13*, 15182–15188.
- (26) Fujiwara, T.; Zgierski, M. Z.; Lim, E. C. *Phys. Chem. Chem. Phys.* **2011**, *13*, 6779–6783.
- (27) Zachariasse, K. A.; Druzhinin, S. I.; Kovalenko, S. A.; Senyushkina, T. *J. Chem. Phys.* **2009**, *131*, 224313–10.
- (28) Druzhinin, S. I.; Ernsting, N. P.; Kovalenko, S. A.; Lustres, L. P.; Senyushkina, T. A.; Zachariasse, K. A. *J. Phys. Chem. A* **2006**, *110*, 2955–2969.
- (29) Pigliucci, A.; Vauthey, E.; Rettig, W. *Chem. Phys. Lett.* **2009**, *469*, 115–120.
- (30) Chudoba, C.; Kummrow, A.; Dreyer, J.; Stenger, J.; Nibbering, E. T. J.; Elsaesser, T.; Zachariasse, K. A. *Chem. Phys. Lett.* **1999**, *309*, 357–363.
- (31) Okamoto, H.; Inishi, H.; Nakamura, Y.; Kohtani, S.; Nakagaki, R. *J. Phys. Chem. A* **2001**, *105*, 4182–4188.
- (32) Kwok, W. M.; Ma, C.; Phillips, D.; Matousek, P.; Parker, A. W.; Towrie, M. *J. Phys. Chem. A* **2000**, *104*, 4188–4197.
- (33) Kwok, W. M.; George, M. W.; Grills, D. C.; Ma, C. S.; Matousek, P.; Parker, A. W.; Phillips, D.; Toner, W. T.; Towrie, M. *Angew. Chem., Int. Ed.* **2003**, *42*, 1826–1830.
- (34) Kwok, W. M.; Ma, C.; George, M. W.; Grills, D. C.; Matousek, P.; Parker, A. W.; Phillips, D.; Toner, W. T.; Towrie, M. *Phys. Chem. Chem. Phys.* **2003**, *5*, 1043–1050.
- (35) Kwok, W. M.; Ma, C.; George, M. W.; Grills, D. C.; Matousek, P.; Parker, A. W.; Phillips, D.; Toner, W. T.; Towrie, M. *Photochem. Photobiol. Sci.* **2007**, *6*, 987–994.
- (36) McCamant, D. W.; Kukura, P.; Yoon, S.; Mathies, R. A. *Rev. Sci. Instrum.* **2004**, *75*, 4971–4980.
- (37) Kukura, P.; McCamant, D. W.; Yoon, S.; Wandschneider, D. B.; Mathies, R. A. *Science* **2005**, *310*, 1006–1009.
- (38) Kukura, P.; McCamant, D. W.; Mathies, R. A. *Annu. Rev. Phys. Chem.* **2007**, *58*, 461–488.
- (39) Yoshizawa, M.; Hattori, Y.; Kobayashi, T. *Phys. Rev. B* **1994**, *49*, 13259–13262.
- (40) Yoshizawa, M.; Kurosawa, M. *Phys. Rev. A* **2000**, *6001*, 013808.
- (41) Weigel, A.; Ernsting, N. P. *J. Phys. Chem. B* **2010**, *114*, 7879–7893.
- (42) Weigel, A.; Dobryakov, A.; Klaumunzer, B.; Sajadi, M.; Saalfrank, P.; Ernsting, N. P. *J. Phys. Chem. B* **2011**, *115*, 3656–3680.
- (43) Mallick, B.; Lakshman, A.; Radhakrishna, V.; Umapathy, S. *Curr. Sci.* **2008**, *95*, 1551–1559.
- (44) Umapathy, S.; Mallick, B.; Lakshman, A. *J. Chem. Phys.* **2010**, *133*, 024505–6.
- (45) Mehlenbacher, R.; Lyons, B.; Wilson, K.; Yong, D.; McCamant, D. M. *J. Chem. Phys.* **2009**, *131*, 244512.
- (46) Laimgruber, S.; Schachenmayr, H.; Schmidt, B.; Zinth, W.; Gilch, P. *Appl. Phys. B* **2006**, *85*, 557–564.
- (47) Megerle, U.; Pugliesi, I.; Schriever, C.; Sailer, C.; Riedel, E. *Appl. Phys. B* **2009**, *96*, 215–231.
- (48) McCamant, D. W.; Kukura, P.; Mathies, R. A. *Appl. Spectrosc.* **2003**, *57*, 1317–1323.
- (49) Deckert, V.; Kiefer, W. *Appl. Spectrosc.* **1992**, *46*, 322–328.
- (50) Knoll, P.; Singer, R.; Kiefer, W. *Appl. Spectrosc.* **1990**, *44*, 776–782.
- (51) Challa, J. R.; Du, Y.; McCamant, D. W. *Appl. Spectrosc.* **2012**, *66*, 227–232.
- (52) Barone, V. *J. Chem. Phys.* **2004**, *120*, 3059–3065.
- (53) Barone, V. *J. Chem. Phys.* **2005**, *122*, 014108.
- (54) Frisch, M. J.; Trucks, G. W.; Schlegel, H. B.; Scuseria, G. E.; Robb, M. A.; Cheeseman, J. R.; Montgomery, J. A., Jr.; Vreven, T.; Kudin, K. N.; Burant, J. C.; Millam, J. M.; Iyengar, S. S.; Tomasi, J.; Barone, V.; Mennucci, B.; Cossi, M.; Scalmani, G.; Rega, N.; Petersson, G. A.; Nakatsuji, H.; Hada, M.; Ehara, M.; Toyota, K.; Fukuda, R.; Hasegawa, J.; Ishida, M.; Nakajima, T.; Honda, Y.; Kitao, O.; Nakai, H.; Klene, M.; Li, X.; Knox, J. E.; Hratchian, H. P.; Cross, J. B.; Bakken, V.; Adamo, C.; Jaramillo, J.; Gomperts, R.; Stratmann, R. E.; Yazyev, O.; Austin, A. J.; Cammi, R.; Pomelli, C.; Ochterski, J. W.; Ayala, P. Y.; Morokuma, K.; Voth, G. A.; Salvador, P.; Dannenberg, J. J.; Zakrzewski, V. G.; Dapprich, S.; Daniels, A. D.; Strain, M. C.; Farkas, O.; Malick, D. K.; Rabuck, A. D.; Raghavachari, K.; Foresman, J. B.; Ortiz, J. V.; Cui, Q.; Baboul, A. G.; Clifford, S.; Cioslowski, J.; Stefanov, B. B.; Liu, G.; Liashenko, A.; Piskorz, P.; Komaromi, I.; Martin, R. L.; Fox, D. J.; Keith, T.; Al-Laham, M. A.; Peng, C. Y.; Nanayakkara, A.; Challacombe, M.; Gill, P. M. W.; Johnson, B.; Chen, W.; Wong, M. W.; Gonzalez, C.; Pople, J. A. *Gaussian 03*, revision C.02; Gaussian, Inc.: Wallingford, CT, 2004.
- (55) Druzhinin, S. I.; Ernsting, N. P.; Kovalenko, S. A.; Lustres, L. W.; Senyushkina, T. A.; Zachariasse, K. A. *J. Phys. Chem. A* **2006**, *110*, 2955–2969.
- (56) Kwok, W. M.; Gould, I.; Ma, C.; Puranik, M.; Umapathy, S.; Matousek, P.; Parker, A. W.; Phillips, D.; Toner, W. T.; Towrie, M. *Phys. Chem. Chem. Phys.* **2001**, *3*, 2424–2432.

- (57) Okamoto, H.; Inishi, H.; Nakamura, Y.; Kohtani, S.; Nakagaki, R. *Chem. Phys.* **2000**, *260*, 193–214.
- (58) Wilson, E. B. J.; Decius, J. C.; Cross, P. C. *Molecular Vibrations: The Theory of Infrared and Raman Vibrational Spectra*; Dover: New York, 1955.
- (59) Fonseca, T.; Kim, H. J.; Hynes, J. T. *J. Mol. Liq.* **1994**, *60*, 161–200.
- (60) Kim, H. J.; Hynes, J. T. *J. Photochem. Photobiol., A* **1997**, *105*, 337–343.
- (61) Fonseca, T.; Kim, H. J.; Hynes, J. T. *J. Photochem. Photobiol., A* **1994**, *82*, 67–79.
- (62) Changenet, P.; Plaza, P.; Martin, M. M.; Meyer, Y. H. *J. Phys. Chem. A* **1997**, *101*, 8186–8194.
- (63) Shreve, A. P.; Mathies, R. A. *J. Phys. Chem.* **1995**, *99*, 7285–7299.
- (64) Chardin, A.; Berthelot, M.; Laurence, C.; Morris, D. G. *J. Phys. Org. Chem.* **1995**, *8*, 626–628.
- (65) Dudev, T.; Bobadova-Parvanova, P.; Pencheva, D.; Galabov, B. *J. Mol. Struct.* **1997**, *437*, 427–433.
- (66) Saito, T.; Yamakawa, M.; Takasuka, M. *J. Mol. Spectrosc.* **1981**, *90*, 359–366.
- (67) Stoyanov, S. S. *J. Phys. Chem. A* **2010**, *114*, 5149–5161.
- (68) Varadwaj, P. R.; Bangal, P. R. *J. Mol. Struct.: THEOCHEM* **2005**, *730*, 23–32.
- (69) Skinner, M. W.; Thompson, H. W. *J. Chem. Soc.* **1955**, 487–489.
- (70) Eaton, G.; Penanunez, A. S.; Symons, M. C. R.; Ferrario, M.; McDonald, I. R. *Faraday Discuss.* **1988**, *85*, 237–253.
- (71) Zhao, G. J.; Han, K. L. *J. Comput. Chem.* **2008**, *29*, 2010–2017.
- (72) Aschaffenburg, D. J.; Moog, R. S. *J. Phys. Chem. B* **2009**, *113*, 12736–12743.
- (73) Chaban, G. M. *J. Phys. Chem. A* **2004**, *108*, 4551–4556.